JCTC Journal of Chemical Theory and Computation

Trends in Aromatic Oxidation Reactions Catalyzed by Cytochrome P450 Enzymes: A Valence Bond Modeling

Sason Shaik,* Petr Milko, Patric Schyman, Dandamudi Usharani, and Hui Chen

The Institute of Chemistry and the Lise Meitner-Minerva Center for Computational Quantum Chemistry, The Hebrew University of Jerusalem, 91904 Jerusalem, Israel

Abstract: The mixed density functional theory (DFT) and valence bond study described herein focuses on the activation of 17 benzene derivatives by the active species of Cytochrome P450, so-called Compound I (Cpd I), as well as by the methoxy radical, as a potentially simple model of Cpd I (Jones, J. P.; Mysinger, M.; Korzekwa, K. R. *Drug Metab. Dispos.* **2002,** *30,* 7−12). Valence bond modeling is employed to rationalize the P450 mechanism and its spin-state selectivity from first principles of electronic structure and to predict activation energies independently, using easily accessible properties of the reactants: the singlet−triplet excitation energies, the ionization potentials of the aromatics, and the electron affinity of Cpd I and/or of the methoxy radical. It is shown that the valence bond model rationalizes all the mechanistic aspects and predicts activation barriers (for 35 reactions) with reasonable accuracy compared to the DFT barriers with an average deviation of ± 1.0 kcal·mol^{-1} (for DFT barriers, see: Bathelt, C. M.; Ridder, L.; Mulholland, A. J.; Harvey, J. N. *Org. Biomol. Chem.* **2004,** *2,* 2998−3005). The valence bond modeling also reveals the mechanistic similarities between the P450 Cpd I and methoxy reactions and enables one to make predictions of barriers for reactions from other studies.

Introduction

Cytochrome P450s are heme enzymes that metabolize and biosynthesize essential compounds,[1] by use of a high-valent iron-oxo porphyrin cation−radical complex, Por$^{+\cdot}$Fe(IV)O, so-called Compound I (Cpd I).[1−3] Among these reactions are the activation of aromatic compounds, Scheme 1, to arene oxides, phenols, and ketones, which influences the bioavail-ability of drugs (phenols) and may also contribute to carcinogenicity via DNA mutations (arene oxides).[4] The relationship between the various products became intriguing when mechanistic investigations[4b,c] led to the conclusion that the arene oxide is an obligatory intermediate in this reaction and the phenol and ketone are its byproducts.[4d,e] However, new evidence suggested alternative pathways proceeding through radical and/or cationic Meisenheimer tetrahedral intermediates, as shown in Scheme 1.[1a,2e,5] These mechanistic studies have also generated many relative reactivity and

Scheme 1. Intermediates and Products during Arene Oxidation by P450 Cpd I
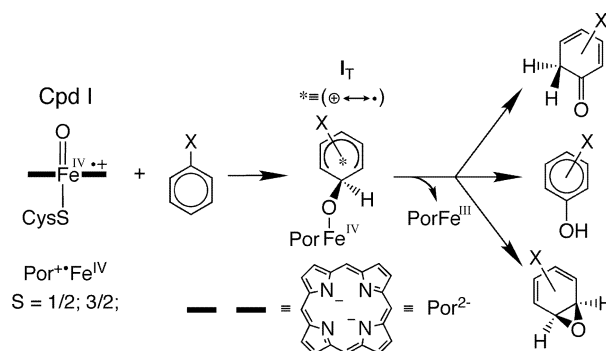
regioselectivity data,[2e,5,6] which were addressed by a few groups[5,7,8] and reviewed.

The advent of density functional theory (DFT) has enabled testing of these mechanistic alternatives on model systems[9] and within native proteins (CYP 2C9)[10] using density functional theory/molecular mechanics (DFT/MM) calcula-

---

* Corresponding author. E-mail: sason@yfaat.ch.huji.ac.il. Tele-phone: +972-2-6585909.

tions. Thus, all the calculations support the intermediacy of a Meisenheimer tetrahedral intermediate (I_T),[3e,9,10] as the source of all products, and reveal the π-activation step as rate determining for all the products. Additionally, the DFT calculations have produced a wealth of information on the dependence of these rate-controlling barriers on the aromatic ring substituents and on the positional selectivity. By and large, these model studies reproduced the observed experimental trends.[9b−e]

In addition the calculations revealed several intriguing features, which we address herein: (i) unlike alkane hydroxylation, which proceeds via the two spin states of Cpd I ($S = 1/2$; $3/2$),[3] aromatic activation preferentially takes place via the lower-energy doublet state ($S = 1/2$);[9] (ii) the transition states were found to have a hybrid nature with radical and cationic characters;[9,10] (iii) this hybrid character is retained in the tetrahedral intermediates, which is neither fully cationic nor radicalar;[10] (iv) relative to benzene, both electron-donating and -withdrawing substituents decrease the barrier for para position attack;[6a,9c] and (v) in accord with experiment,[6a] a significant preference is observed for para regioselectivity even with electron-withdrawing substituents, e.g., NO_2,[9c,d] which in electrophilic substitution normally leads to meta regioselectivity.

This abundance of knowledge has created the need for establishing order; namely, the outlining of broad generalizations as well as the creation of more intuitive interfaces between experimental and theoretical data. Several studies were published, which employed the methoxy radical as a Cpd I mimic[8a,b,9d] or used a "hybrid" Hammett substituent parameter,[9c] to describe reactivity of Cpd I with aromatic substrates. In the present study, we use valence bond (VB) modeling of aromatic oxidation by P450, with an aim of deriving the above trends from first principles and thereby generating a general theoretical framework that organizes the reactivity patterns. The VB diagram model was previously applied successfully to address reactivity patterns in alkane hydroxylation and thioether sulfoxidation by P450.[11] The Manchester group[12] has extended the VB modeling to include also bond activation by nonheme oxo-iron reagents. The VB diagram model[13] has a few merits: It reveals the origins of the barrier, describes the formation of transition states and reaction intermediates, and allows the prediction of barrier heights and structure−reactivity relationships. As shall be shown, the modified application of the VB diagram model used herein enabled us to go beyond previous treatments[11,12] and derive the above reactivity patterns from first principles based on physically clear predictors. Thus, the modified VB model rationalizes the hybrid nature of the transition states and intermediates[9c,d] as well as the different barriers of the spin states during the reactions with Cpd I and the relationship to radical attacks by MeO•.[8a] Furthermore, this VB model leads to expressions that estimate barrier heights from easily accessible reactant properties, such as singlet−triplet promotion energies, ionization potential (IP), and electron affinity (EA).

Our focus is the series of reactions in Scheme 2a, studied before by Bathelt et al.[9c] using DFT (B3LYP) calculations. As noted by the authors,[9c] some of these molecules would

Scheme 2. Studied Reactions of Ar-X Molecules with (a) Cpd I and (b) MeO•
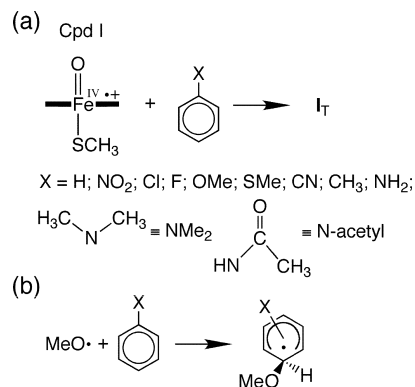
undergo preferentially other reactions and were used by them for the sole purpose of modeling structure−reactivity relationships. Our goal herein is the same. Note that unlike our usual choice to represent the cysteinate axial ligand by HS^-,[3a,b,d,e] we use here CH_3S^- in keeping with the original study of Bathelt et al.[9c] Furthermore, since, Bathelt et al.[9c] showed that the effect of bulk polarity makes a contribution to the barrier, which is virtually substituent independent, and DFT/MM calculations of benzene activation by P450 2C9, confirmed this incremental contribution of bulk polarity to the barrier,[10] we restrict our study to the gas-phase model reactions.[14] To test the reactivity patterns of aromatic activation by a simple radical, we use the reaction series with MeO• in Scheme 2b. The so derived VB insight will be demonstrated by attempts to predict trends in other molecules.

Methods

Software. The starting points for the calculations of the Cpd I addition were the structures published in study of Bathelt et al.[9c] which employed Jaguar 4.2.[15a] Single-point calculations of the barriers for π-activation were carried out with Gaussian 03 and 09,[15b,c] at these structures (communicated by Harvey). In two cases (X = NMe_2, Cl), the calculated energies did not correspond to those obtained in the original study, but upon reoptimization of the TSs with Jaguar 7.6,[15d] the correct structures were obtained, as shown by the new calculated barriers matching the original study. As such, we were able to create a data set wherein all barriers are calculated using the same methods and procedures, thus removing nonsystematic errors, which might be contributed by use of different software packages and procedures (see Supporting Information, Tables S1 and S2).

We note here that in the original study,[9c] the authors optimized Cpd I(CH_3S^-) within C_s symmetry constraints. Removing this constraint and optimizing at C_1 lowers the energy of Cpd I(CH_3S^-) by 4.0 kcal·mol^{-1} (see Supporting Information, Table S3; note that the electronic structure of the Cpd I(CH_3S^-) shows more pronounced mixing of the sulfur p_z orbital with the porphyrin a_{2u} orbital in C_s symmetry than in C_1 one).[3b] Since this adds a constant to the barriers and it had no effect on the quality of the VB modeling, we present here the barriers with the C_s constrained Cpd I(CH_3S^-) to stay as close as possible to the original study.[9c]
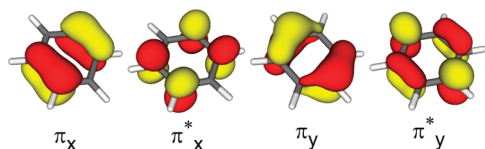
Valence Bond Modeling

J. Chem. Theory Comput., Vol. 7, No. 2, 2011 **329**

Figure 1. The π and π^*-type orbitals of benzene.

The VB modeling with the C_1 data is given in the Supporting Information (Table S17).

Since we will later attempt to make predictions on cases calculated with a Cpd I model having a HS$^-$ axial ligand, we tested the ligand effect (HS$^-$ vs CH$_3$S$^-$) on the benzene activation, using the same basis sets as Bathelt et al.[9c] We found that the axial ligand effect on the calculated benzene activation is small (0.2 kcal·mol^{-1}) if Cpd I(CH$_3$S$^-$) is indeed constrained to C_s symmetry. Because of this constraint, we did not perform zero point energy (ZPE) correction, which is anyway small for this kind of reaction.

All the MeO$^\bullet$ reactions as well as IP's and EA's were studied using Gaussian 09 geometry optimization.[15c] Charge-transfer values (see Figure 3) in the transition state were calculated with NBO 3.1 as implemented in Gaussian 03.[15c,16]

Functional and Basis Sets. Thus, as in the original study,[9c] all the calculations were performed using the unrestricted hybrid density functional method UB3LYP.[17] Geometry optimizations (without constraints) were performed with the LACV3P basis set on iron and 6-31G* on the rest of the atoms (basis set BSI).[17,18,19a,b] Subsequently, single point calculations were done on the optimized geometries using BSII, which corresponds to LACV3P(Fe)/6-311+G** (rest).[19c,d] The so computed reaction barriers for the Cpd I/arene series (Scheme 2a) were within ±0.6 kcal·mol^{-1} of those reported in the study of Bathelt et al. with an exception for addition to the meta position in which the deviation was 1.3 kcal·mol^{-1} (see Supporting Information, Tables S1 and S2).[9c] The MeO$^\bullet$ transition states were optimized with the 6-31G* basis set, and energy was corrected using the 6-311+G** basis set.

Auxiliary Data for VB Modeling. As shall be seen, the VB modeling relies on two properties of the arene molecules, the vertical IP and singlet−triplet $\pi\pi^*$ excitation energies, ΔE_{ST}. Further, it requires also EA's of Cpd I and of the methoxy radical as input data. We used the experimental IP values of the studied substrates from the NIST database.[20] In parallel we ascertained that DFT reproduces these IP's well (see Supporting Information for details).

To be consistent with calculated IP's (see Supporting Information, Figure S1 and Table S7), the B3PW91/6-311++G** level was chosen to obtain the vertical ΔE_{ST} values.[17a,19c,d,21] Based on the π-type orbitals in Figure 1, there are generally two closely lying excitation types, which can be obtained from DFT and involve π_y to π^*_y and π_x to π^*_x excitations. The $\pi_x \rightarrow \pi^*_x$ excitation energy is insensitive to the nature of the substituents, while the $\pi_y \rightarrow \pi^*_y$ excitation is strongly dependent on the substituent, giving generally lower values for the latter excitation. A plot of the calculated $\Delta E_{ST}(\pi_y \rightarrow \pi^*_y)$ excitations against adiabatic experimental values[22] shows identical trends (see Supporting Information,
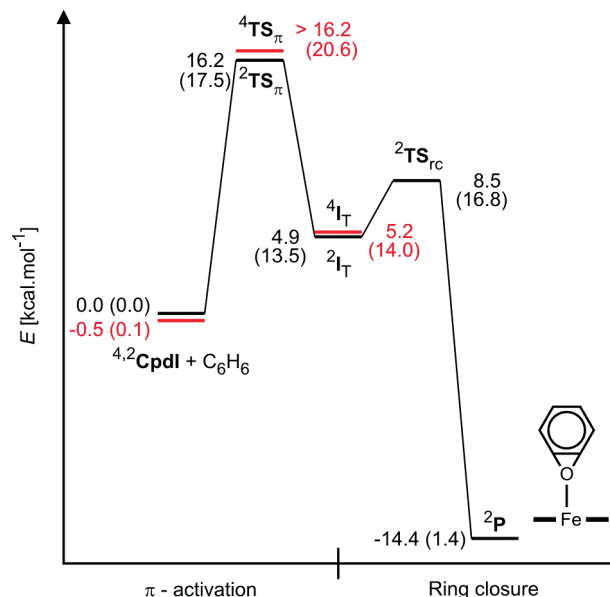

Figure 2. B3LYP potential energy profiles for the epoxidation of benzene by ^{4,2}Cpd I (the quartet-state species are marked in red). All energies are in kcal·mol^{-1} relative to isolated ^{2}Cpd I and benzene. Each species has two energy values, corresponding to BSII (this work and ref 9c) and in parentheses to LACVP(Fe)/6-31G(rest) from ref 9a.

Figure S2), and with the exception of X = NO$_2$, the calculated vertical values are about 20 ± 3 kcal·mol^{-1} higher than the experimental adiabatic values. The calculated $\Delta E_{ST}(\pi_y \rightarrow \pi^*_y)$ value for benzene 102.2 kcal·mol^{-1} is in excellent agreement with the CCSD(T)/cc-pV∞Z calculated datum, 104.4 kcal·mol^{-1}, for the $^3B_{1u}$ state[23a] and close to a spin-coupled valence bond (SCVB) calculated value, 97.3 kcal·mol^{-1}.[23b] From absorption peak progressions for benzene and fluorobenzene in magnetic induced singlet−triplet excitations studied by Evans,[22b] it is possible to deduce that the vertical excitation energies are ∼94−97 kcal·mol^{-1} compared with the DFT calculated values 102.2 and 101.9 kcal·mol^{-1}.

The EAs of Cpd I and MeO$^\bullet$ are constant quantities for the respective reaction series studied here, but to be consistent with past calculations,[3a,b,d,e] B3LYP was used to obtain the vertical EA of Cpd I using C_s geometry,[9c] leading to EA = 64.9 kcal·mol^{-1}. The unconstrained C_1 structure has a lower EA value of 60.6 kcal·mol^{-1}, while the Cpd I with HS$^-$ ligand has EA = 67.9 kcal·mol^{-1}. The vertical EA of MeO$^\bullet$ was determined using single point calculations at CCSD(T) level of theory,[24] CCSD(T)/aug-cc-pVQZ//UB3LYP/6-311+G**, and leads to EA = 32.1 kcal·mol^{-1}.[25]

All the data generated in this study are shown in the Supporting Information document. For space economy, the following sections will focus on the key data only.

Results

Energy Profiles. Figure 2 shows the energy profiles for the activation of benzene by Cpd I, using the recalculated data based on geometries from Bathelt at el.[9c] and the previous data of de Visser and Shaik using Cpd I(HS$^-$).[9a] Despite the differences in the representations of Cpd I and

330 *J. Chem. Theory Comput., Vol. 7, No. 2, 2011*

Shaik et al.

X	d_{CO}	d_{FeO}	d_{FeS}	Q_{CT}	ρ_{ArX}
H	1.890	1.730	2.378	0.35	-0.46
Cl	1.902	1.731	2.361	0.34	-0.44
F	1.950	1.717	2.386	0.33	-0.38
CN	1.939	1.719	2.369	0.24	-0.34
NO_2	1.847	1.727	2.411	0.21	-0.41
NMe_2	2.052	1.693	2.389	0.46	-0.45
OMe	2.006	1.710	2.369	0.40	-0.40
NH_2	2.077	1.693	2.384	0.43	-0.41
CH_3	2.028	1.701	2.396	0.32	-0.35
SMe	1.951	1.711	2.389	0.38	-0.44
N-acetyl	2.064	1.701	2.391	0.33	-0.35

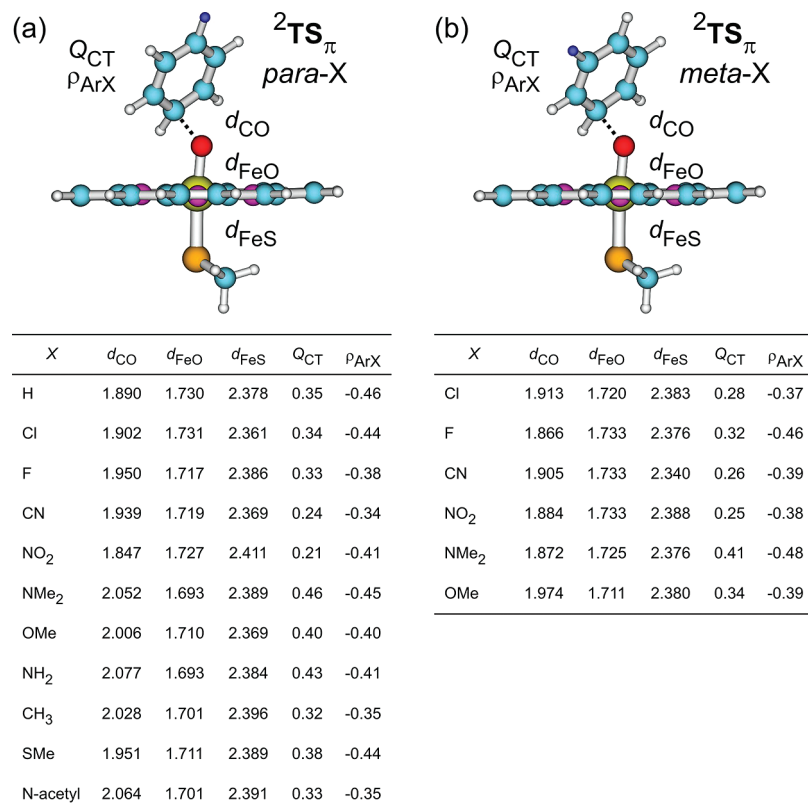| X	d_{CO}	d_{FeO}	d_{FeS}	Q_{CT}	ρ_{ArX}
Cl	1.913	1.720	2.383	0.28	-0.37
F	1.866	1.733	2.376	0.32	-0.46
CN	1.905	1.733	2.340	0.26	-0.39
NO_2	1.884	1.733	2.388	0.25	-0.38
NMe_2	1.872	1.725	2.376	0.41	-0.48
OMe	1.974	1.711	2.380	0.34	-0.39

Figure 3. Optimized $^2TS_\pi$ species during π-activation of arenes by Cpd I, key geometric distances (in Å), degrees of charge transfer (Q_{CT}) from the arene to Cpd I, and spin densities on the arenes (ρ_{ArX}). TSs for (a) para attack and (b) meta attack. Color code: yellow, orange, red, purple, and blue correspond to iron, sulfur, oxygen, nitrogen, and carbon, respectively. Dark blue represents the position of the X substituents.

the basis sets, the two sets of relative energy values are mechanistically consistent. Thus, the initial step involves the π-activation of benzene by ^{4,2}Cpd I via two transition states, $^{4,2}TS_\pi$. In both studies, the quartet species $^4TS_\pi$ lies about 0.6−3.3 kcal·mol^{-1} above the corresponding doublet transition state. Recalculating the barrier with Cpd I(HS$^-$) and the same basis sets as those in Bathelt et al.[9c] gave a 1.8 kcal·mol^{-1} preference for the doublet over the quartet state. In all cases, these transition states lead to the corresponding tetrahedral Meisenheimer intermediates ($^{4,2}I_T$), and again the doublet-state species is lower in energy.[9a−c] The intermediate in turn undergoes a variety of reactions (see Scheme 1), and Figure 2 shows the ring closure to the benzene-oxide, via $^2TS_{rc}$, which represents the simplest reaction pathway toward a product. As found by de Visser and Shaik,[9a] the quartet-state profile continues to lie above the doublet state. In both studies the doublet-state barrier to ring closure is smaller than those for the π-activation step. All other barriers for the conversion of ^2I_T to the other two products (phenol and ketone, in Scheme 1) are also small.[9a,c] Therefore, the VB modeling will focus hereafter on the π-activation step in the doublet spin state. Since none of the follow-up steps is rate controlling, their VB modeling will be largely waved (with the exception of the qualitative representation in Figure 7a of the simplest follow-up step).

Transition States for π-Activation by Cpd I and MeO$^•$. Key geometric features of the $^2TS_\pi$ species for π-activation of the various substituted benzene derivatives, studied herein, are shown in Figure 3. Figure 4 displays the

corresponding species for the reactions with the MeO$^•$ radical (Scheme 2b), which focused more on para attacks. For each TS_π in Figures 3 and 4, we indicated three bond distances and the quantities: Q_{CT}, the amount of charge transferred (CT) from the arene to Cpd I in the TS, and ρ_{ArX}, the spin density value on the ArX molecule in the TS.

Inspection of Figure 3 shows that: (i) all the $^2TS_\pi$ species are uniformly side-on types; this uniformity is important since side-on and face-on barriers have small differences, which would have added nonsystematic contributions into the data set; (ii) all the $^2TS_\pi$s possess a hybrid radical/cationic character in the arene; (iii) the O···C bond lengths in the transition states vary in the range of 1.847−2.077 Å; (iv) the $^2TS_\pi$ species with para electron-releasing substituents have 'earlier' structures with longer C···O bond lengths; (v) the para substituted $^2TS_\pi$ species are significantly earlier than the meta substituted ones; and (vi) the amount of charge transferred from the arene to Cpd I, Q_{CT}, depends on the substituent; it is larger for the electron-releasing substituents with maximum of $Q_{CT} = 0.46$e for NMe_2, and the effect is more significant for the para substituted $^2TS_\pi$ species. Figure 4 shows similar trends in Q_{CT} values and O···C distances but within a narrower range compared with the Cpd I reactions.

Barriers for π-Activation by Cpd I and MeO$^•$ and Trends. Table 1 collects the π-activation barriers for the P450 reactions as well as those calculated for the reactions with MeO$^•$, along with two properties of the arene: the IP's and the singlet−triplet $\pi\pi^*$ excitations, $\Delta E_{ST}(\pi\pi^*)$.
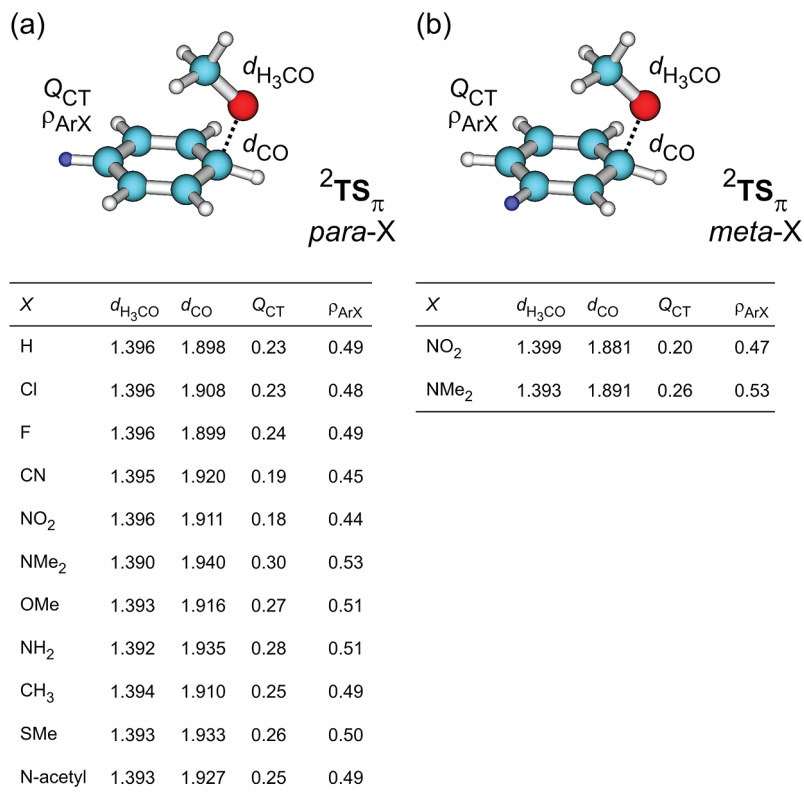
Valence Bond Modeling

J. Chem. Theory Comput., Vol. 7, No. 2, 2011 **331**

Figure 4. Optimized $^2TS_\pi$ species during π-activation of arenes by MeO$^\bullet$, key geometric distances (in Å), degrees of charge transfer (Q_{CT}) from the arene to Cpd I, and spin densities on the arenes (ρ_{ArX}). TSs for (a) para attack and meta attack. Color code: red and blue correspond to oxygen and carbon, respectively. Dark blue represents the position of the X substituents.

(a)

X	d_{H_3CO}	d_{CO}	Q_{CT}	ρ_{ArX}
H	1.396	1.898	0.23	0.49
Cl	1.396	1.908	0.23	0.48
F	1.396	1.899	0.24	0.49
CN	1.395	1.920	0.19	0.45
NO$_2$	1.396	1.911	0.18	0.44
NMe$_2$	1.390	1.940	0.30	0.53
OMe	1.393	1.916	0.27	0.51
NH$_2$	1.392	1.935	0.28	0.51
CH$_3$	1.394	1.910	0.25	0.49
SMe	1.393	1.933	0.26	0.50
N-acetyl	1.393	1.927	0.25	0.49

(b)

X	d_{H_3CO}	d_{CO}	Q_{CT}	ρ_{ArX}
NO$_2$	1.399	1.881	0.20	0.47
NMe$_2$	1.393	1.891	0.26	0.53

Table 1. Experimental IP's, Calculated $\pi\pi^*$ Singlet–Triplet Excitations, $\Delta E_{ST}(\pi\pi^*)$, and UB3LYP/BSII/UB3LYP/BSI Calculated Barriers, $\Delta E^\ddagger$ (kcal·mol^{-1}), for π-Activation of Ar-X by Cpd I and MeO$^\bullet$ on para and meta Positions

X	IP$_{exp}$[a] (kcal·mol^{-1})	$\Delta E_{ST}(\pi\pi^*)$[b] (kcal·mol^{-1})	$\Delta E^\ddagger$, CpdI (kcal·mol^{-1})[c] para	meta	$\Delta E^\ddagger$, MeO$^\bullet$ (kcal·mol^{-1})[c] para	meta
H	213.1	102.2	16.2		7.9	
Cl	209.4	97.3	15.3	15.7	7.4	
F	214.0	101.9	15.2	16.3	7.5	
CN	225.3	89.3	14.9	15.9	7.6	
NO$_2$	232.0	87.1	14.2	15.3	8.1	9.0
NMe$_2$	174.1	89.4	9.6	16.8	3.3	8.1
OMe	193.7	97.6	13.2	15.3	5.7	
NH$_2$	185.4	91.5	11.0		4.2	
CH$_3$	205.0	99.0	15.0		7.0	
SMe	187.7	89.5	12.6		5.3	
N-acetyl	195.1	90.7	13.6		5.9	

[a] Experimental values from the NIST database. [b] Calculated values (B3PW91/6-311++G**). [c] Without ZPE correction.
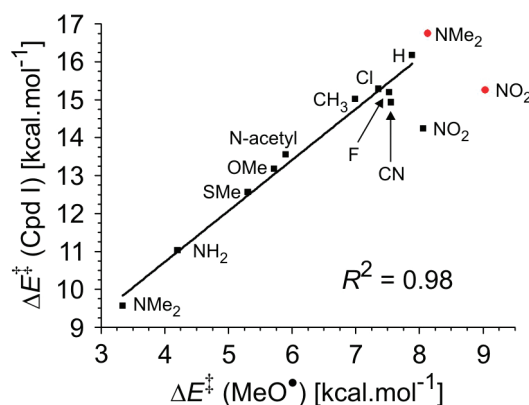

Figure 5. A plot of the barriers for π-activation of arenes by Cpd I vs MeO$^\bullet$. The red circles are barriers for meta-position attacks (without ZPE correction). The R^2 value corresponds to the points of the best fit for the attack on the para position (excluding the NO$_2$–Ph data).

Inspection of Table 1 shows the following trends: (i) The P450 barriers are sensitive to the substituent on the benzene ring and vary between 9.6 kcal·mol^{-1} (Ph-NMe$_2$) to 16.2 kcal·mol^{-1} (benzene); (ii) the barriers for attack on the meta positions are generally larger than those for the para position in which the most pronounced effect is observed for the Cpd I addition to Ph-NMe$_2$ (9.6 and 16.8 kcal·mol^{-1} for the addition on para and meta position, respectively); (iii) the barriers for MeO$^\bullet$ para-position attacks are much smaller than the P450 values and vary in a narrower range of 3.3−8.1 kcal·mol^{-1}; and (iv) with the exception of X = NO$_2$ in the MeO$^\bullet$ series, in both P450 and MeO$^\bullet$ series, the attacks on

para positions of the substituents have lower barriers relative to benzene. Indeed, activation barriers of the Cpd I addition and the methoxy radical addition are in good mutual correlation, with the exception of nitrobenzene (Figure 5).

The $\Delta E^\ddagger$ values for the para-position attack (by either Cpd I or MeO$^\bullet$), with the exception of those for the most electron-withdrawing substituents (CN, NO$_2$), show a linear dependence on the IP values of the arene.[12d] Similarly, part of the data correlates linearly with the $\Delta E_{ST}(\pi\pi^*)$ values. However, none of these two physical properties can by itself correlate with all of the data. By contrast, all the P450 barrier set can be correlated nicely with a hybrid quantity, IP +
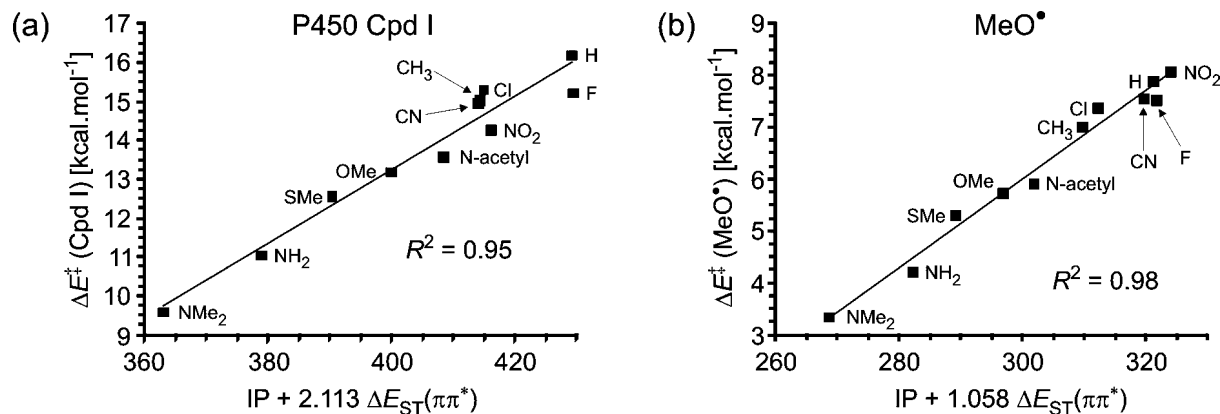
Figure 6. A plot of the π-activation barriers vs: (a) IP + $2.113\Delta E_{ST}(\pi\pi^*)$, for the P450 reactions and (b) IP + $1.058\Delta E_{ST}(\pi\pi^*)$ for the MeO$^\bullet$ reactions. (IP's taken from NIST, and the fit is based on Maple 13 software).

$2.113\Delta E_{ST}(\pi\pi^*)$, as seen in Figure 6a, and for the MeO$^\bullet$ set with IP + $1.058\Delta E_{ST}(\pi\pi^*)$, as shown in Figure 6b. The double correlation was obtained by a standard fit routine, as is implemented in Maple 13 program package (see Supporting Information, Table S9). This hybrid correlation retrieves the similar one found by Bathelt et al.,[9c] using Hammett substituent parameters. The correlation follows also the hybrid character seen in the charge transfer and spin density in the P450 transition states in Figure 3.

Discussion

The above computational results show a few intriguing trends for the P450 reactions:[9] (i) The computed P450 profiles show that the doublet-state mechanism is lower in energy relative to the quartet state; (ii) the π-activation step has a higher lying barrier than the following rearrangement steps; (iii) the $^2TS_\pi$ species for π-activation as well as the corresponding tetrahedral intermediates, ^2I_T, have hybrid radical/cationic characters (Figure 3), which depend on the ring substituent; (iv) the π-activation barriers are sensitive to the substituent on the benzene ring, the lowest barrier is obtained for the Cpd I addition to the para position of Ph-NMe$_2$, but all the para substituents are found to lower the barrier with respect to the unsubstituted benzene; (v) the barriers for attack on the meta positions are generally larger than those for the para position, even for the electronic-withdrawing substituents which generally direct electrophilic reagents for meta attacks; (vi) the π-activation barriers can be correlated reasonably well with a mixed quantity made from a combination of the IP of the arene and its singlet–triplet excitation energy, $\Delta E_{ST}(\pi\pi^*)$; and (vii) the barriers for MeO$^\bullet$ attacks are much smaller than the P450 values and vary in a narrower range of 3.3–8.1 kcal·mol^{-1}, nevertheless the two barrier sets exhibit a reasonable mutual correlation.

We shall now present a VB modeling of these reactions with an aim of unifying these findings and understanding thereby these reactivity patterns.[13] Subsequently we shall show that the barriers can be calculated from raw data based on the VB model.[11]

VB Modeling. *Energy Profiles Generated from VB Mixing Principles.* Since the follow-up rearrangements of the tetrahedral intermediate have much smaller barriers

compared with the common π-activation step, the modeling will focus on this step up to the Meisenheimer complex intermediate. To facilitate the discussion, we show in Scheme 3, the molecular orbital (MO) and VB representations of Cpd I and some helpful oxidation-state formulations.[11] Scheme 3a shows key MOs of Cpd I: The $\sigma_{FeO}{}^2\pi_{FeO}{}^4\pi^*_{FeO}{}^2$ configuration represents the bonding block and accounts for a σ_{FeO} bond and a $\pi_{FeO}{}^4\pi^*_{FeO}{}^2$ manifold, as in $^3O_2$,[3a,b,d,e,26,27] and spin-up electrons in π^*_{FeO}. The π^*_{FeO} orbitals are considered as "d" orbitals, so that the d-block occupancy is $\delta^2\pi^*_{FeO}{}^2\sigma^*_{xy}{}^0\sigma^*_{z^2}{}^0$. Finally, the porphyrin cation–radical is represented by the singly occupied a$_{2u}$; the double-headed arrow represents spin-down/spin-up arrangements for the doublet/quartet states of Cpd I.

Scheme 3b outlines the correspondence of the MO and VB representations of Cpd I, with the $\delta^2\sigma^*_{xy}{}^0\sigma^*_{z^2}{}^0$ block placed in parentheses. On the left side, we show the bonding block MO configuration, $\sigma_{FeO}{}^2\pi_{FeO}{}^4\pi^*_{FeO}{}^2$. In the VB representation σ_{FeO} is drawn as a line, while in VB the π-block is represented by two resonating three-electron bonds, which span two perpendicular planes, with two spin-up electrons on iron-oxo.[3,11] Finally, the open-shell porphyrin (a$_{2u}{}^1$) is represented by a cation–radical symbol on porphyrin. These VB cartoons will be used hereafter. The reader may note also that each of the resonance structures, in Scheme 3b, looks like Fe^{III}–O$^\bullet$. Nevertheless, because their superposition relays four of the electrons to π_{FeO}-bonding orbitals, this leaves a Fe(d^4) configuration that qualifies as Fe^{IV}O. However, during the reaction the electronic structure gets localized and becomes Fe^{III}–O$^\bullet$.[11c]

Scheme 3c and 3d summarizes some basic conventions of the oxidation-state formalism, which tracks d-electron counts of transition-metal complexes during redox processes. Scheme 3c shows oxidation numbers for Cpd I: the porphyrin has a σ-oxidation number of 2–, the oxo is 2–, and the thiolate is 1–. Since the molecule is neutral, the heme oxidation-state is V, which becomes Por$^{+\bullet}$Fe(IV)O, based on spectroscopic evidence[1,2] for a porphyrin π-cation radical. With Fe(IV), Cpd I will have a d^4 electronic configuration.[3,9] Scheme 3d depicts the iron-aryloxo electromers due to π-attack by Cpd I on the arene. The resulting OAr group has an oxidation number of 1–, and hence the effective oxidation state of the heme becomes IV, which can manifest

Scheme 3. MO and VB Representations of Cpd I[a]
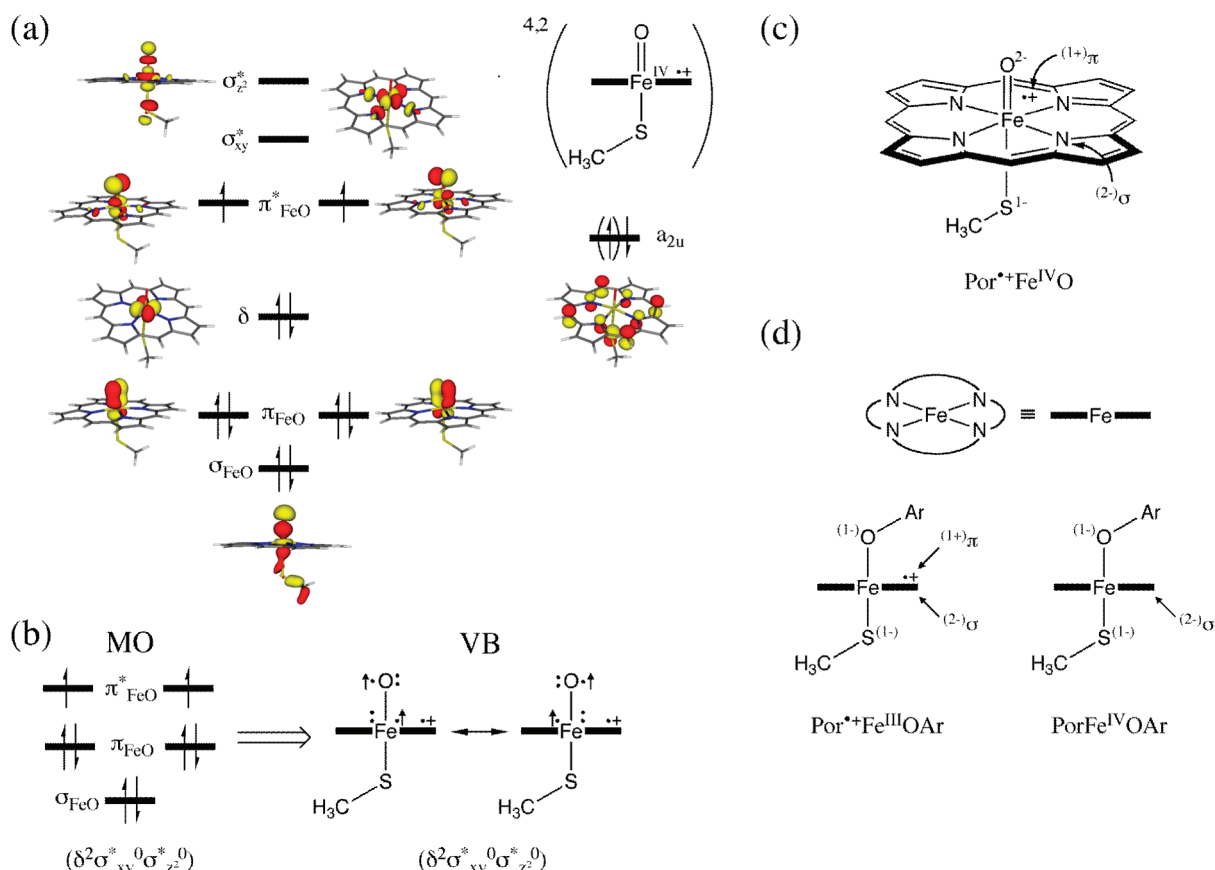
[a] The following represent: (a) Key MO's, (b) MO-VB correspondence of the FeO-bonding block, (c) oxidation numbers in Cpd I, and (d) oxidation numbers in tetrahedral intermediate (I_T).

as PorFe(IV)OAr and/or Por$^{+•}$Fe(III)OAr, with electronic configurations d^4 and/or d^5, respectively. As amply discussed,[3] π-activation by Cpd I leads to two electromeric states for the tetrahedral intermediates,[3e,9a] of the Por$^{+•}$Fe^{III}OAr and PorFe^{IV}OAr types. Since the VB diagrams are very similar for the two electromers[11a] and the latter are usually the more stable in the gas phase, as found to be so in this study, we shall focus only on the latter type.

Figure 7a shows the VB diagram for benzene epoxidation via the doublet spin state. For the sake of economy, the benzene is symbolized by a single Kekulé structure and so is Cpd I. The diagram involves two principal curves for the direct O transfer to the arene. The curves are anchored at the ground states (Ψ_r, Ψ_p) and their two promoted states (Ψ_p^*, $\Psi_{r,CT}^*$). This direct process is, however, catalyzed by an intermediate-state curve ($\Psi_I^*(IV)$) that cuts through the higher energy ridge for direct oxo-transfer and splits the process into side-on π-attack followed by ring closure to form the ferric-arene-oxide product.[11,13b,c] This three-curve VB diagram is a typical case,[11–13] wherein an intermediate state internally facilitates the otherwise more difficult transformation of Ψ_r directly to Ψ_p.

Let us elaborate on the electronic structure of the promoted state for the principal curves: $^2\Psi_{r,CT}^*$ is a state with a mixed CT and covalent structures, which describes the two new O–C bonds that will be formed between the oxo of Cpd I and the arene molecule. To save space,[3e,11] Figure 7a shows

only the main charge-transfer structure, whereas Figure 7b shows explicitly the contributing structures, which combine together to produce eventually the arene oxide in $^2\Psi_p$. There are two equivalent charge-transfer structures, $^2\Phi_{CT}$, which arise by one-electron transfer from the arene to porphyrin$^{+•}$ and where the electrons on the O$^•$ and C$^•$ are coupled to a bond pair across one C–O linkage, while the other linkage has an ionic character (shown by dots). In addition, there is a purely covalent contributor, $^2\Phi_{COV}$, which maintains two covalent C$^•$–$^•$O spin pairs between the arene and the oxo of Cpd I. The charge-transfer structures, $^2\Phi_{CT}$, dominate $^2\Psi_{r,CT}^*$, as indicated in Figure 7a.[28,29] Note that, since the C$^•$–$^•$O bond pairing lowers the oxidation number of the heme to a ferric (Fe^{III}) state, $^2\Psi_{r,CT}^*$ is actually an image state of the ferric-arene oxide product and hence along the reaction coordinate $^2\Psi_{r,CT}^*$ correlates to $^2\Psi_p$, as shown in Figure 7a. In an analogous manner, in the reverse direction, the promoted state, $^2\Psi_p^*$, is formed from $^2\Psi_p$ by an electron transfer from the porphyrin to one of the O–C bonds while pairing the electrons on the arene, and as such, $^2\Psi_p^*$ is the electronic image of the ground state on the other side, $^2\Psi_r$, and the two correlate along the reaction coordinate.

Let us turn now to the intermediate-state curve in Figure 7a. This VB curve which is anchored in $^2\Psi_I^*(IV)$ participates in the π-activation step by forming the Meisenheimer intermediate ^2I_T. Thus, $\Psi_I^*(IV)$ involves an electron shift from iron (from π_{FeO}^*, see Scheme 3a) to porphyrin$^{+•}$ (which
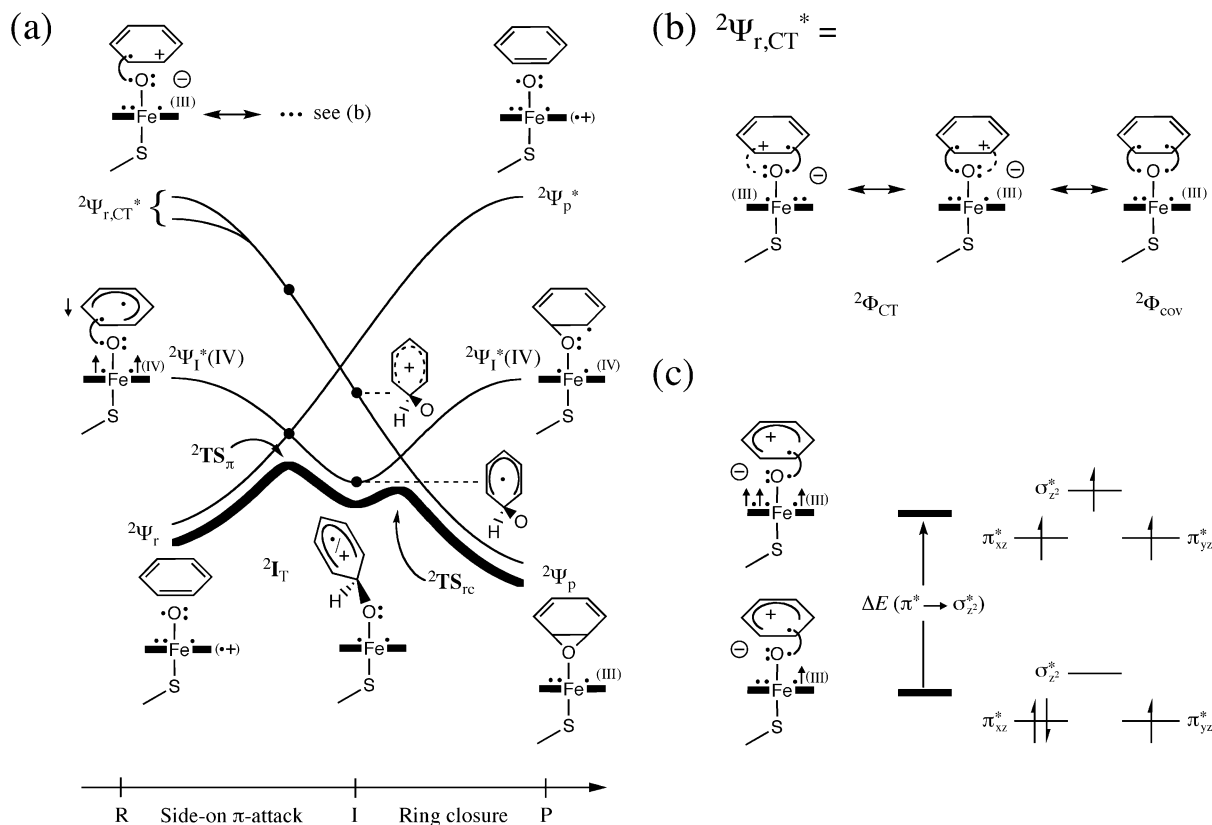
Figure 7. (a) A VB diagram describing the mechanistic scenario during the doublet spin-state conversion of benzene to benzene-oxide via intermediacy of the Meisenheimer intermediate, ^2I_T. (b) A detailed description of the major contributors to the promoted state $^2\Psi_{r,CT}*$. (c) The relative energies of $^2\Psi_{r,CT}*$ and $^4\Psi_{r,CT}*$.

is energetically a small excitation, ca. 5−6 kcal·mol^{-1}).[11c] In addition, the π-system of benzene is promoted to a triplet configuration, while C$^•$ and $^•$O are coupled into a bond pair, which eventually becomes the O−C bond in ^2I_T. Note that $^2\Psi_I*$(IV) is different than the covalent component $^2\Phi_{COV}$ of $^2\Psi_{r,CT}*$, and it also lies lower in energy, since $^2\Phi_{COV}$ involves a costly promotion from the oxygen doubly occupied orbital to porphyrin$^{+•}$ ($\pi_{FeO} \rightarrow a_{2u}$).[28] Thus, $^2\Phi_{COV}$ possesses two C$^•$−$^•$O bond pairs, while $^2\Psi_I*$(IV), wherein the oxo group has three electrons, can form only one C$^•$−$^•$O bond pair, and therefore the latter leads to the Meisenheimer intermediate. On the product side, $^2\Psi_I*$(IV) correlates to an excited state of the product having Fe(IV) and three-electrons in one of the C−O linkages.

The final energy profile in Figure 7a is obtained by the mixing of the three state curves, resulting in a biphasic energy profile, dominated by the intermediate-state curve, with a π-activation phase followed by ring closure. The relative barrier heights are determined by the vertical promotion energies between the intersection states, and since the promotion gap at the ^2I_T junction is much smaller than in the reactant onset, the barrier for the π-activation phase is rate controlling, while at the ring-closure state it is a rather small barrier. Other follow-up steps from the ^2I_T junction, e.g., the formation of phenols, can be described analogously, but they require their own VB diagrams,[13] as they are associated with the migration of the ipso proton to the oxo ligand.[9a]

Nature of the π-Activation Transition State and the Tetrahedral Intermediate. Let us start with the natures of

$^2TS_\pi$ and ^2I_T Figure 7a. The charge-transfer state curve, $^2\Psi_{r,CT}*$ lies not so much higher than the intersection point of the $^2\Psi_r-^2\Psi_I*$(IV) curves, where $^2TS_\pi$ will be formed by mixing of the three state curves. Consequently, $^2TS_\pi$ will exhibit a partial charge transfer from the arene to the Cpd I moiety, to an extent that depends on the arene substituent (X). For example, with X = NMe$_2$ the IP of the arene is the lowest in the series, ca. 58 kcal·mol^{-1} lower than that of nitrobenzene, with the highest IP. As such, the mixing of the charge-transfer state for X = NMe$_2$ will be the most pronounced in the series, while for X = NO$_2$, it would be the least significant, as in fact revealed by the computational results in Figure 3, which shows Q_{CT} values for the various substituents. Similarly, the tetrahedral ^2I_T intermediate will have a hybrid character, with a dominant radical character, but neither fully radical nor fully cationic.

Spin-State Preference. The difference between the doublet and quartet spin processes is depicted in Figure 7c, which shows $^2\Psi_{r,CT}*$ and $^4\Psi_{r,CT}*$ and their energy difference. Thus, in both states we have a PorFe(III)O$^•$−$^•$Ar$^+$ species, which arises by electron transfer from the arene to porphyrin$^{+•}$ while coupling O$^•$ and $^•$C to a bond-pair. However, whereas the PorFe(III) moiety of $^2\Psi_{r,CT}*$ has a $\delta^2\pi^{*2}\pi^{*1}$ d-block configuration, $^4\Psi_{r,CT}*$ is typified by $\delta^2\pi^{*1}\pi^{*1}\sigma^*_{z^2}{}^1$. Thus, $^4\Psi_{r,CT}*$ involves also a $\pi^* \rightarrow \sigma^*_{z^2}$ promotion within the d-block (approximately, 30 kcal·mol^{-1}).[11b] Since the charge-transfer state is rather close to the other two curves, its mixing into $^{2,4}TS_\pi$ can be deduced from simple considerations of perturbation theory. It is thus expected that generally the $^2TS_\pi$ species will have greater mixing and be lower than $^4TS_\pi$.
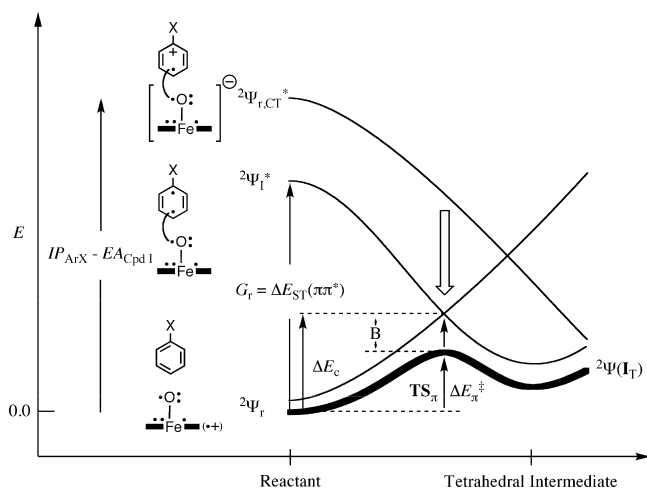
Valence Bond Modeling

J. Chem. Theory Comput., Vol. 7, No. 2, 2011 **335**

Figure 8. A VB diagram for the π-activation step, showing the three state curves and the key quantities that determine the barrier.

Of course, the extent of this spin selectivity is expected to be modulated by the substituent X, such that electron-withdrawing susbstituents, which raise the IP of the arene, will lead to a smaller energy advantage of $^2TS_\pi$ over $^4TS_\pi$ species.

Reactivity Patterns: Using VB Diagrams to Estimate π-Activation Barriers. Figure 8 shows a section of the VB diagram with the reactivity quantities, which are necessary for modeling of the barrier and its variation. The drawings of the species near the curve represent an attack on the para position to the substituent X, and later on we shall generalize this to meta attacks. The figure shows that the barrier is determined largely by the avoided crossing and VB mixing of the reactant and intermediate curves, $^2\Psi_r$ and $^2\Psi_I{}^*$, but the charge-transfer state lying above, $^2\Psi_{r,CT}{}^*$, can also mix and lower the resulting barrier. The simplest expression for the barrier of an elementary step is eq 1:

$$\Delta E_\pi^\ddagger = \Delta E_c - B \qquad (1)$$

Here ΔE_c measures the height of the crossing point of Ψ_r and $^2\Psi_I{}^*$, and B is TS-resonance energy due to the VB mixing of the three curves.

The height of the crossing point reflects the total deformation energies of the two reactants and their Pauli repulsions, which are required to achieve the $^2\Psi_r - {}^2\Psi_I{}^*$ crossing.[30] As usual, the height of the crossing point can be expressed as a fraction (f) of the promotion energy at the reactant side (G_r) leading to eq 2:

$$\Delta E_\pi^\ddagger = fG_r - B \qquad (2)$$

Since the promotion energy is simply the singlet-to-triplet excitation of the arene, eq 2 becomes

$$\Delta E_\pi^\ddagger = f\Delta E_{ST} - B \qquad (3)$$

Recalling that B reflects also the mixing in the charge-transfer state, we expect that this quantity will vary as a function of the relative energy of the transfer state $\Psi_{r,CT}{}^*$ near the crossing point. This energy difference cannot be quantified

computationally, but we should expect that it will change in proportion to the initial energy of $^2\Psi_{r,CT}{}^*$ relative to the ground state, $^2\Psi_r$, and is given by:

$$\Delta E_{CT}(^2\psi_r \rightarrow {}^2\psi_{r,CT}{}^*) = IP_{ArX} - EA_{Cpd\,I} \qquad (4)$$

where IP_{ArX} is the IP of the arene, while $EA_{Cpd\,I}$ is the EA of Cpd I.

In summary, we expect that the barrier will be determined by the variation of the singlet-to-triplet excitation of the arene, with a secondary influence of the ionization potential of the arene. Equations 3 and 4 can be used to estimate barriers for the series of reactions of this study. Since the reaction resembles a radical attack, we can use $f = 0.3$ or 1/3, as done previously for H abstraction for radicals.[11a,31] The only missing quantity is then B. However, having f and ΔE_{ST}, we can extract the B values needed to reproduce the DFT-calculated barriers:

$$B = f\Delta E_{ST} - \Delta E_\pi^\ddagger \qquad (5)$$

These data are shown in the fifth column of Table 2. Thus, for example, using the DFT-calculated barrier ($\Delta E_\pi^\ddagger$) of benzene, the corresponding ΔE_{ST} value (102.2 kcal·mol^{-1}), and $f = 0.3$, we get B(benzene) $= 14.5$ kcal·mol^{-1}, and the same procedure leads to $B = 17.2$ kcal·mol^{-1} for the N,N-dimethylaniline. Other B values are derived similarly.

But we can do better than that, by modeling the B values based on the understanding that these quantities reflect the mixing of the corresponding charge-transfer states. Using perturbation theory, this mixing will be inversely proportional to the energy gap between the charge transfer $\Psi_{r,CT}{}^*$ and the crossing point in Figure 8 and will be proportional to the matrix element that couples the states. Since the energy gap of the crossing point is expected to be proportional to $IP_{ArX} - EA_{Cpd\,I}$ in eq 4 and the matrix element for coupling these states is gauged by the odd electron density on the carbon site where O−C bond is made, we can use the following simple expression for B_X for a given substituent X, relative to B_H for the unsubstituted benzene:

$$B_X = B_H\{[\rho_X(IP_H - EA_{Cpd\,I})]/[\rho_H(IP_X - EA_{Cpd\,I})]\} \qquad (6)$$

Here ρ_X and ρ_H are, respectively, the spin densities at the sites of attack of the X-substituted arene vs benzene, in the corresponding triplet states. Thus, all we need is to have B_H, the value for benzene, and derive from it all the other B_X values. The so calculated B values are collected in the sixth column of Table 2.

Before looking at these results it is instructive to inspect the spin densities, which are depicted in Figure 9 for representative substituents (for remaining ones see Supporting Information, Figures S3 and S4). For most of the substituents, the lowest triplet state is due to $\pi_y \rightarrow \pi^*_y$ excitation (consult Figure 1 for the orbitals), and Figure 9a shows the spin densities for three cases. It is apparent that the site of the highest spin density is the para position, whereas the meta position has negligible spin density. Figure 9b shows the triplet spin densities corresponding to the $\pi_x \rightarrow \pi^*_x$ excitation. Here it is seen that the spin density is largest at the meta and ortho positions, but the meta spin

Table 2. Reactivity Factors and VB Estimated B_X Values and Barriers for the para Position Attacks by Cpd I on ArX Molecules

X	IP^a (kcal·mol^{-1})	ΔE_{ST} $(\pi\pi^*)^b$ (kcal·mol^{-1})	$\rho_{x,para}{}^c$	$B_X{}^d$ (DFT)	$B_X{}^e$ (VB)	$\Delta E_\pi{}^\ddagger$ (VB)^f (kcal·mol^{-1})	$\Delta E_\pi{}^\ddagger$ (DFT) (kcal·mol^{-1})
H	213.1	102.2	0.86	14.5	14.5	16.2	16.2
Cl	209.4	97.3	0.80	13.9	13.8	15.4	15.3
F	214.0	101.9	0.83	15.4	13.9	16.7	15.2
CN	225.3	89.3	0.75	11.9	11.7	15.1	14.9
NO$_2$	232.0	87.1	0.76	11.9	11.4	14.8	14.2
NMe$_2$	174.1	89.4	0.76	17.2	17.4	9.4	9.6
OMe	193.7	97.6	0.82	16.1	15.9	13.4	13.2
NH$_2$	185.4	91.5	0.76	16.4	15.7	11.7	11.0
CH$_3$	205.0	99.0	0.89	14.7	15.9	13.8	15.0
SMe	187.7	89.5	0.75	16.2	15.2	13.5	12.6
N-acetyl	195.1	90.7	0.75	13.8	14.4	13.0	13.6

^{a} Experimental values from the NIST database corresponding to vertical ionization. ^{b} See Table 1. ^{c} Spin density localized at the para carbon of ArX in the triplet state. ^{d} B_X is defined by eq 5; $B = f\Delta E_{ST} - \Delta E_\pi{}^\ddagger$. ^{e} B_X (VB) is derived from eq 6. ^{f} MUE = 0.6 kcal·mol^{-1}.
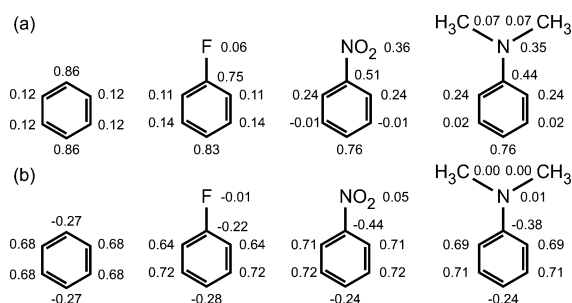
Figure 9. Spin density distributions in the triplet states of a few Ar-X molecules in: (a) the $\pi_y \rightarrow \pi^*_y$ and (b) the $\pi_x \rightarrow \pi^*_x$ states.

density is still smaller than the para value in Figure 9a. It is clear therefore from eqs 4 and 6 that the barriers will be generally larger for meta position attack on the ring, which is what the calculations here and elsewhere[9c,d] generally show, albeit not always.[9d]

The VB barriers of the para attacks (seventh column in Table 2) were modeled using eqs 4 and 6 with experimental IP_X values, $EA_{Cpd\ I} = 64.9$ kcal·mol^{-1} and $f = 0.3$. Thus, for example, using the $IP_H - EA_{Cpd\ I}$ for benzene (148.2 kcal·mol^{-1}), the $IP_X - EA_{Cpd\ I}$ for X = NMe$_2$ (109.2 kcal·mol^{-1}), and the corresponding ρ_H and ρ_{NMe2} values (0.86 and 0.76, respectively), we obtain $B_{NMe2} = 17.4$ kcal·mol^{-1} and the corresponding barrier 9.4 kcal·mol^{-1} compared with the DFT-calculated datum of 9.6 kcal·mol^{-1}. Other data in Table 2 (columns sixth and seventh) were derived in the same manner.

We note that Table 2 is one of a few almost equally successful modeling sets made with $f = 0.3$ and 1/3 and theoretical and experimental IP_X values; all these attempts give very similar results and are relegated to the Supporting Information (Tables S10−12). As shown by the data in Table 2, the VB barriers (column seventh) model the DFT results (column eighth) quite well with a mean unsigned error of 0.6 kcal·mol^{-1}. Moreover, the trends in the B_X values (sixth column) modeled by eq 6 are close to the values that are required to reproduce the DFT barriers (eq 5). Thus, our modeling of B_X as a quantity based on the mixing of the charge-transfer state into the transition state appears to be quite reasonable and consistent. In both series, the largest B_X is found for X = NMe$_2$, in good accord with the finding

of the largest Q_{CT} for this substituent in Figure 3. Similarly, the smallest B_X is found for X = NO$_2$, in agreement with the smallest Q_{CT} for this substituent in Figure 3.

The simplest expression to derive the B values for meta attacks is shown in eq 7:

$$B_{X,m} = B_{X,p}[\rho_{X,m}/\rho_{X,p}] \qquad (7)$$

which relates the $B_{X,m}$ value to corresponding para value, assuming that the only factor that varies is the relative spin densities in these positions, $\rho_{X,m}/\rho_{X,p}$, all else being constant. Since the meta attack will mix the two triplet states, $\pi_y \rightarrow \pi^*_y$ and $\pi_x \rightarrow \pi^*_x$, we can use the corresponding spin densities in Figure 9b vs a, to derive the $B_{X,m}$ values. Using eq 7, the predicted meta attack barriers are larger than those for the para attack by 1.5−4.9 kcal·mol^{-1}, whereas the corresponding DFT values are 0.4−2.1 kcal·mol^{-1} (except X = NMe$_2$; see Table 1). In the most deviant case, eq 7 predicts a rise of the meta barrier by 4.7 kcal·mol^{-1} vis-à-vis the DFT calculated 7.2 kcal·mol^{-1}. Obviously eq 7 yields the correct direction in the barrier change, because $B_{X,m} < B_{X,p}$, but it certainly is much oversimplified to provide exact changes in the barrier.

VB Modeling of Reactivity for MeO• Attacks. The VB diagram for arene activation by MeO• is shown in Figure 10. Here we are concerned only with the π-activation step, which bears similarities to the activation by Cpd I. Indeed, as in Figure 8, here we find the state where the ArX molecule is excited to a triplet and is coupled via a C•−•O bond pair and the charge-transfer state, $^2\Psi_{r,CT}*$, which will mix with the other state curves and generate a TS$_\pi$ species with a mixed character. However, since MeO• has a low EA (36.5 kcal·mol^{-1})[20] compared with Cpd I, the charge-transfer state is high lying here in Figure 10 and will mix to a smaller extent into the TS wave function. This is indeed born out by the DFT calculations in Figures 3 vs 4, which shows that the Q_{CT} quantities are always smaller in the MeO• transition states.

The barrier can be modeled using eq 4 with $f = 0.3$ (see Supporting Information, Tables S14−16). The various B_X values can be derived from eq 4 by using the DFT barriers, and alternatively, it can be modeled using eq 8:

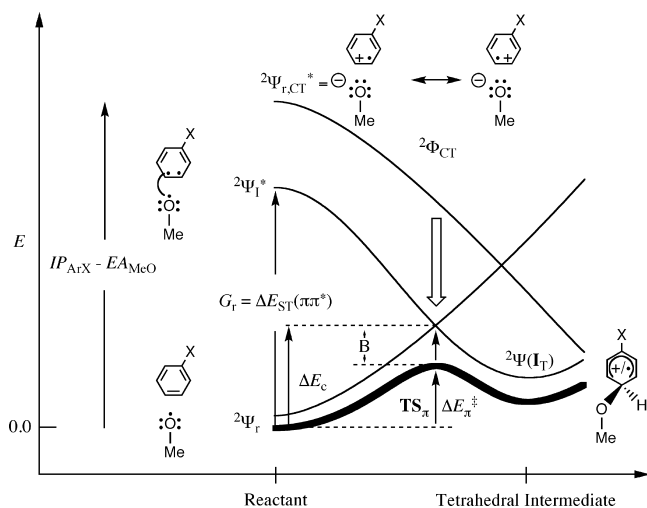$$B_X = B_H\{[\rho_X(IP_H - EA_{MeO})]/[\rho_H(IP_X - EA_{MeO})]\} \qquad (8)$$

Valence Bond Modeling

J. Chem. Theory Comput., Vol. 7, No. 2, 2011 **337**

Figure 10. A VB diagram describing the π-activation step for MeO$^\bullet$ attack on the para position of arenes.

Table 3. Reactivity Factors and VB Estimated B Values and Barriers for para Position Attacks by MeO$^\bullet$ on X-Substituted Benzene Derivatives[a]

X	B_X^b (DFT)	B_X^c (VB)	$\Delta E_\pi^\ddagger$ (VB)[d] (kcal·mol^{-1})	$\Delta E_\pi^\ddagger$ (DFT) (kcal·mol^{-1})
H	22.8	22.8	7.9	7.9
Cl	21.8	21.6	7.5	7.4
F	23.0	21.9	8.7	7.5
CN	19.2	18.6	8.2	7.6
NO$_2$	18.1	18.2	7.9	8.1
NMe$_2$	23.5	25.7	1.2	3.3
OMe	23.6	24.3	5.0	5.7
NH$_2$	23.3	23.8	3.7	4.2
CH$_3$	22.7	24.7	5.0	7.0
SMe	21.6	23.1	3.8	5.3
N-acetyl	21.3	22.1	5.1	5.9

[a] IP's and $\Delta E_{ST}(\pi\pi^*)$ are those which are given in Table 2. [b] B_X (DFT) is defined by eq 5; $B = f\Delta E_{ST} - \Delta E_\pi^\ddagger$. [c] B_X (VB) is derived from eq 8. [d] MUE = 1.0 kcal·mol^{-1}.

which is analogous to eq 6, with one difference that the EA of Cpd I is replaced by that of MeO$^\bullet$ (calculated vertical EA$_{MeO}$ = 32.1 kcal·mol^{-1}).

All the data are assembled in Table 3, which shows a few trends: First, the B_X values are invariably larger than those for the Cpd I series, in accord with the tighter transition states produced by DFT, in Figure 4 vs 3.

The B_X values estimated from eq 8 and the corresponding VB barriers are close to the DFT-derived ones within a mean unsigned error of 1.0 kcal·mol^{-1}. Furthermore, using eq 7 for the meta B_X values leads to the same conclusion as before, namely that $B_{X,m} < B_{X,p}$. Thus, the VB modeling captures the essence of the two reactions and shows their close relationships.

Addition of Cpd I or MeO$^\bullet$ to aromatic compounds (ArX) generates transition states with similar electronic structures on the substrate, involving both charge and radical characters. Inspection of the transition states (Figures 3 and 4) shows that spin localization is not affected by the reagent identity, whereas the charge-transfer values are more pronounced for transition states generated by Cpd I attack. This larger charge transfer can be attributed to higher EA of Cpd I compared to the methoxy radical. Similar transition-state characters for

Table 4. Predicted Activation Energies in kcal·mol^{-1} for the Cpd I Addition to Halogenated Anilines and Benzenes

substrate	position	predicted (VB)[d]	calculated (DFT)
C$_6$F$_6$		9.4[a]	8.9[b]
C$_6$Cl$_6$		14.8[a]	15.0[b]
1,2-difluoro-benzene	3, 6	16.6	16.6[c]
1,2-difluoro-benzene	4, 5	18.8	15.2[c]
aniline	4	11.7	11.0[c]
2-fluoro-aniline		13.7	11.7[c]
2,6-difluoro-aniline		11.7	12.0[c]
2,3,6-trifluoro-aniline		12.9	11.8[c]

[a] Using Cpd I (HS$^-$). To gauge the B values for these substrates, the VB model used EA$_{Cpd\ I}$ = 67.9 kcal·mol^{-1} for Cpd I (HS$^-$) and the corresponding barrier for benzene activation (15.8 kcal·mol^{-1}) calculated with UB3LYP/LACV3P(Fe)/6-311+G**(rest)//UB3LYP/LACV3P(Fe)/6-31G*(rest). Using the Cpd I (CH$_3$S$^-$) leads to 14.6 and 9.7 kcal·mol^{-1}. [b] See ref 32. [c] See ref 9c. [d] MUE = 1.3 kcal·mol^{-1}.

both reagents are also reflected in the VB modeling. The transition-state energies are gauged by the singlet–triplet energy gap and the resonance energy B_X; the latter quantity reflects also influence by the ability of a substrate to give off an electron and the ability of an oxidant to accept an electron. The VB model thus successfully describes both reaction types and predicts activation energies in reasonably good agreement with the DFT values. It further reveals that the methoxy radical can mimic Cpd I for studies of oxygen addition, as assumed in the pioneering study of Jones et al.[8a]

Making Independent Predictions Using the VB model. The VB model allows us to try making independent predictions of activation energies and compare these with values calculated by DFT in the literature. Some of these predictions are collected in Table 4.

Thus, as can be seen from Table 4, Hackett et al.[32] calculated by DFT, barriers of 15.0 and 8.9 kcal·mol^{-1}, respectively, for oxygenation of C$_6$Cl$_6$ and C$_6$F$_6$ by Cpd I too while using the singlet–triplet excitation energies and eq 6, the VB model predicts with good agreement, the values of 14.8 kcal·mol^{-1} and 9.4 kcal·mol^{-1} (C$_6$Cl$_6$ and C$_6$F$_6$). Further, Bathelt et al.[9c] calculated DFT barriers for oxidation of halogenated aniline and 1,2-difluoro-benzene, which compared favorably with experimental data.[5b] It is apparent from Table 4 that the VB model predicts the barriers are in reasonable agreement with DFT.

Whereas the model predicts reasonable barrier values, its ability to predict regioselectivity is somewhat less effective. Thus, in the case of 1,2-difluoro-benzene, Bathelt et al.[9c] predicted a regioselectivity ratio (4,5/3,6) of 63/37 in agreement with the experimental result (67/33).[5b] The VB model predicts on the other hand a preference for 3,6. In other substrates studied theoretically and experimentally,[9d,33] the VB model predicted correctly two cases ((4/6)-methyl-3-fluoro-aniline) and incorrectly for the other two (3-fluoro-aniline and 2-methyl-3-fluoro-aniline). Part of the problem originates in the difficulties to describe all the closely lying triplet states of polysubstituted substrates with DFT. Another part is, of course, due to the fact that regioselectivity is often determined by barrier differences of sub kcal·mol^{-1}, while the accuracy of the VB model is of the order of $\sim$1 kcal·mol^{-1}. One can think of ways to improve the predictive

338 *J. Chem. Theory Comput., Vol. 7, No. 2, 2011*

Shaik et al.

ability of model by averaging the spin densities for all the closely lying states, but this will affect the simplicity and clarity of the model.

Conclusion

The above study describes a valence-bond modeling approach to the mechanism of arene activation by P450 Cpd I and a methoxy radical. Interestingly, while the VB model is applied here in a manner reminiscent of the quantitative structure−activity relationship methodology,[9e] the VB parameters derive from first principles of electronic structure and, as such, are not arbitrary but rather have physical significance. Thus, VB modeling shows the origins of the barriers for both reaction series and the nature of the corresponding transitions states. Additionally, it elucidates the underling reasons for the stepwise mechanism and the spin selectivity for the reactions of Cpd I. Finally, the model is used to predict barriers for the rate-determining π activation step, with reasonable accuracy compared to the DFT values (mean unsigned deviation for 35 barriers is 1.0 kcal·mol^{-1}), based on easily accessible properties, such as the IPs and singlet−triplet excitation energies of the substrates and the EA of Cpd I. Much order is thus provided by the VB model into P450 chemistry.[11]

Supporting Information Available: Cartesian coordinates of the all structures described in this work, Tables with group spin densities and charges, and figures with various correlations are posted. This information is available free of charge via the Internet at http://pubs.acs.org.

References

(1) (a) Sono, M.; Roach, M. P.; Coulter, E. D.; Dawson, J. H. *Chem. Rev.* **1996**, *96*, 2841–2887. (b) *Cytochrome P450: Structure, Mechanism and Biochemistry*, 3rd ed.; Ortiz de Montellano, P. R., Ed.; Kluwer Publishers/Plenum Press: New York, 2005. (c) Guengerich, F. P. *Chem. Res. Toxicol.* **2001**, *14*, 611–650. (d) Ortiz de Montellano, P. R.; De Voss, J. J. *Nat. Prod. Rep.* **2002**, *19*, 477–494. (e) Guengerich, F. P. *Annu. Rev. Pharmacol. Toxicol.* **1999**, *39*, 1–17. (f) Groves, J. T. *Proc. Natl. Acad. Sci. U.S.A.* **2003**, *100*, 3569–3574.

(2) See, e.g.: (a) Groves, J. T. *J. Inorg. Biochem.* **2006**, *100*, 434–447. (b) Schlichting, I.; Berendzen, J.; Chu, K.; Stock, A. M.; Maves, S. A.; Benson, D. E.; Sweet, R. M.; Ringe, D.; Petsko, G. A.; Sligar, S. G. *Science* **2000**, *287*, 1615–1622. (c) Groves, J. In *Cytochrome P450: Structure, Mechanism, and Biochemistry*, 3rd ed.; Ortiz de Montellano, P. R., Ed.; Springer: New York, 2005; Ch. 1, pp 1−43. (d) Denisov, I. G.; Makris, T. M.; Sligar, S. G.; Schlichting, I. *Chem. Rev.* **2005**, *105*, 2253–2277. (e) Ortiz de Montellano, P. R. In *Cytochrome P450: Structure, mechanisms, and biochemistry*, 2nd ed.; Ortiz de Montellano, P. R., Ed.; Plenum Press: New York, 1995; Ch. 8, pp 245−303.

(3) (a) Shaik, S.; de Visser, S. P. In *Cytochrome P450: Structure, Mechanisms, and Biochemistry*, 3rd ed.; Ortiz de Montellano, P. R., Ed.; Springer: New York, 2005; Ch. 2, pp 45−85. (b) Shaik, S.; Kumar, D.; de Visser, S. P.; Altun, A.; Thiel, W. *Chem. Rev.* **2005**, *105*, 2279–2328. (c) Yoshizawa, K. *Coord. Chem. Rev.* **2002**, *226*, 251–259. (d) Meunier, B.; de Visser, S. P.; Shaik, S. *Chem. Rev.* **2004**, *104*, 3947–3980. (e) Shaik, S.; Cohen, S.; Wang, Y.; Chen, H.; Kumar, D.; Thiel, W. *Chem. Rev.* **2010**, *110*, 949–1017.

(4) (a) Boyland, E.; Sims, P. *Biochem. J.* **1965**, *95*, 780–787. (b) Jerina, D.; Daly, J.; Witkop, B.; Zaltzman-Nirenberg, P.; Udenfriend, S. *Arch. Biochem. Biophys.* **1968**, *128*, 176–183. (c) Jerina, D.; Daly, J. *Science* **1974**, *185*, 573–582. (d) Jerina, D.; Daly, J.; Witkop, B.; Zaltzman-Nirenberg, P.; Udenfriend, S. *J. Am. Chem. Soc.* **1968**, *90*, 6525–6527. (e) Jerina, D.; Daly, J.; Witkop, B.; Zaltzman-Nirenberg, P.; Udenfriend, S. *Biochemistry* **1970**, *9*, 147–156.

(5) (a) Korzekwa, K. R.; Swinney, D. C.; Trager, W. F. *Biochemistry* **1989**, *28*, 9019–9027. (b) Rietjens, I. M. C. M.; Soffers, A.; Veeger, C.; Vervoort, J. *Biochemistry* **1993**, *32*, 4801–4812. (c) Hanzlik, R.; Hogberg, K.; Judson, C. *Biochemistry* **1984**, *23*, 3048–3055.

(6) (a) Safari, N.; Bahadoran, F.; Hoseinzadeh, M. R.; Ghiasi, R. *J. Porphyrins Phthalocyanines* **2000**, *4*, 285–291. (b) Cnubben, N. H.; Peelen, S.; Borst, J. W.; Vervoort, J.; Veeger, C.; Rietjens, I. M. C. M. *Chem. Res. Toxicol.* **1994**, *7*, 590–598.

(7) (a) Zakharieva, O.; Grodzicki, M.; Trautwein, A. X.; Veeger, C.; Rietjens, I. *J. Biol. Inorg. Chem.* **1996**, *1*, 192–204. (b) Zakharieva, O.; Grodzicki, M.; Trautwein, A.; Veeger, C.; Rietjens, I. *Biophys. Chem.* **1998**, *73*, 189–203.

(8) (a) Jones, J. P.; Mysinger, M.; Korzekwa, K. R. *Drug Metab. Dispos.* **2002**, *30*, 7–12. (b) Dowers, T. S.; Rock, D. A.; Perkins, B. N. S.; Jones, J. P. *Drug Metab. Dispos.* **2004**, *32*, 328–332. (c) Korzekwa, K. R.; Trager, W.; Gouterman, M.; Spangler, D.; Loew, G. H. *J. Am. Chem. Soc.* **1985**, *107*, 4273–4279.

(9) (a) de Visser, S. P.; Shaik, S. *J. Am. Chem. Soc.* **2003**, *125*, 7413–7424. (b) Bathelt, C. M.; Ridder, L.; Mulholland, A. J.; Harvey, J. N. *J. Am. Chem. Soc.* **2003**, *125*, 15004–15005. (c) Bathelt, C. M.; Ridder, L.; Mulholland, A. J.; Harvey, J. N. *Org. Biomol. Chem.* **2004**, *2*, 2998–3005. (d) Rydberg, P.; Ryde, U.; Olsen, L. *J. Chem. Theory Comput.* **2008**, *4*, 1369–1377. (e) Rydberg, P.; Vasanthanathan, P.; Oostenbrink, C.; Olsen, L. *ChemMedChem* **2009**, *4*, 2070–2079.

(10) Bathelt, C. M.; Mulholland, A. J.; Harvey, J. N. *J. Phys. Chem. A* **2008**, *112*, 13149–13156.

(11) (a) Shaik, S.; Kumar, D.; de Visser, S. P. *J. Am. Chem. Soc.* **2008**, *130*, 10128–10140. (b) Shaik, S.; Wang, Y.; Chen, H.; Song, J.; Meir, R. *Faraday Discuss.* **2010**, *145*, 49–70. (c) Shaik, S.; Lai, W.; Chen, H.; Wang, Y. *Acc. Chem. Res.* **2010**, *43*, 1154–1165.

(12) (a) Latifi, R.; Bagherzadeh, M.; de Visser, S. P. *Chem.—Eur. J.* **2009**, *15*, 6651–6662. (b) de Visser, S. P. *J. Am. Chem. Soc.* **2010**, *132*, 1087–1097. (c) de Visser, S. P. *J. Am. Chem. Soc.* **2006**, *128*, 15809–15818. (d) Kumar, D.; Karamzadeh, B.; Narahari Sastry, G.; de Visser, S. P. *J. Am. Chem. Soc.* **2010**, *132*, 7656–7667.

(13) (a) Shaik, S. *J. Am. Chem. Soc.* **1981**, *103*, 3692–3701. (b) Shaik, S.; Shurki, A. *Angew. Chem., Int. Ed.* **1999**, *38*, 586–

625. (c) Shaik, S.; Hiberty, P. C. In *A Chemist's Guide to Valence Bond Theory*; John Wiley & Sons Inc: Hoboken, NJ, 2008; Ch. 6, pp 116−192.

(14) This 'constant' bulk polarity effect can change however, from reaction to reactions, see: de Visser, S. P.; Ogliaro, F.; Sharma, P. K.; Shaik, S. *Angew. Chem., Int. Ed.* **2002**, *41*, 1947−1951.

(15) (a) *Jaguar 4.2* Schrodinger, Inc.: Portland, OR, 2002. (b) Frisch, M. J.; Trucks, G. W.; Schlegel, H. B.; Scuseria, G. E.; Robb, M. A.; Cheeseman, J. R.; Montgomery, J. A., Jr.; Vreven, T.; Kudin, K. N.; Burant, J. C.; Millam, J. M.; Iyengar, S. S.; Tomasi, J.; Barone, V.; Mennucci, B.; Cossi, M.; Scalmani, G.; Rega, N.; Petersson, G. A.; Nakatsuji, H.; Hada, M.; Ehara, M.; Toyota, K.; Fukuda, R.; Hasegawa, J.; Ishida, M.; Nakajima, T.; Honda, Y.; Kitao, O.; Nakai, H.; Klene, M.; Li, X.; Knox, J. E.; Hratchian, H. P.; Cross, J. B.; Bakken, V.; Adamo, C.; Jaramillo, J.; Gomperts, R.; Stratmann, R. E.; Yazyev, O.; Austin, A. J.; Cammi, R.; Pomelli, C.; Ochterski, J. W.; Ayala, P. Y.; Morokuma, K.; Voth, G. A.; Salvador, P.; Dannenberg, J. J.; Zakrzewski, V. G.; Dapprich, S.; Daniels, A. D.; Strain, M. C.; Farkas, O.; Malick, D. K.; Rabuck, A. D.; Raghavachari, K.; Foresman, J. B.; Ortiz, J. V.; Cui, Q.; Baboul, A. G.; Clifford, S.; Cioslowski, J.; Stefanov, B. B.; Liu, G.; Liashenko, A.; Piskorz, P.; Komaromi, I.; Martin, R. L.; Fox, D. J.; Keith, T.; Al-Laham, M. A.; Peng, C. Y.; Nanayakkara, A.; Challacombe, M.; Gill, P. M. W.; Johnson, B.; Chen, W.; Wong, M. W.; Gonzalez, C.; Pople, J. A. *Gaussian 03*, revision E.01; Gaussian, Inc.: Wallingford CT, 2004. (c) Frisch, M. J.; Trucks, G. W.; Schlegel, H. B.; Scuseria, G. E.; Robb, M. A.; Cheeseman, J. R.; Scalmani, G.; Barone, V.; Mennucci, B.; Petersson, G. A.; Nakatsuji, H.; Caricato, M.; Li, X.; Hratchian, H. P.; Izmaylov, A. F.; Bloino, J.; Zheng, G.; Sonnenberg, J. L.; Hada, M.; Ehara, M.; Toyota, K.; Fukuda, R.; Hasegawa, J.; Ishida, M.; Nakajima, T.; Honda, Y.; Kitao, O.; Nakai, H.; Vreven, T.; Montgomery, Jr., J. A.; Peralta, J. E.; Ogliaro, F.; Bearpark, M.; Heyd, J. J.; Brothers, E.; Kudin, K. N.; Staroverov, V. N.; Kobayashi, R.; Normand, J.; Raghavachari, K.; Rendell, A.; Burant, J. C.; Iyengar, S. S.; Tomasi, J.; Cossi, M.; Rega, N.; Millam, N. J.; Klene, M.; Knox, J. E.; Cross, J. B.; Bakken, V.; Adamo, C.; Jaramillo, J.; Gomperts, R.; Stratmann, R. E.; Yazyev, O.; Austin, A. J.; Cammi, R.; Pomelli, C.; Ochterski, J. W.; M artin, R. L.; Morokuma, K.; Zakrzewski, V. G.; Voth, G. A.; Salvador, P.; Dannenberg, J. J.; Dapprich, S.; Daniels, A. D.; Farkas, Ö.; Foresman, J. B.; Ortiz, J. V.; Cioslowski, J.; Fox, D. J. *Gaussian 09*, revision A.02; Gaussian, Inc.: Wallingford, CT, 2009. (d) *Jaguar 7.6*; Schrodinger, LLC: New York, 2009.

(16) (a) Foster, J. P.; Weinhold, F. *J. Am. Chem. Soc.* **1980**, *102*, 7211−7218. (b) Reed, A. E.; Curtiss, L. A.; Weinhold, F. *Chem. Rev.* **1988**, *88*, 899−926.

(17) (a) Becke, A. D. *Phys. Rev. A: At., Mol., Opt. Phys.* **1988**, *38*, 3098−3100. (b) Becke, A. D. *J. Chem. Phys.* **1992**, *96*, 2155−2160. (c) Becke, A. D. *J. Chem. Phys.* **1992**, *97*, 9173−9177. (d) Becke, A. D. *J. Chem. Phys.* **1993**, *98*, 5648−5652. (e) Lee, C.; Yang, W.; Parr, R. G. *Phys. Rev. B: Condens. Matter Mater. Phys.* **1988**, *37*, 785−789.

(18) LACV3P is generated in Jaguar 7.6 from LACVP; Hay, P. J.; Wadt, W. R. *J. Chem. Phys.* **1985**, *82*, 299−308.

(19) (a) Ditchfield, R.; Hehre, W. J.; Pople, J. A. *J. Chem. Phys.* **1971**, *54*, 724−728. (b) Francl, M. M.; Pietro, W. J.; Hehre, W. J.; Binkley, J. S.; DeFrees, D. J.; Pople, J. A.; Gordon, M. S. *J. Chem. Phys.* **1982**, *77*, 3654−3665. (c) Raghavachari, K.; Binkley, J. S.; Seeger, R.; Pople, J. A. *J. Chem. Phys.* **1980**, *72*, 650−654. (d) McLean, A. D.; Chandler, G. S. *J. Chem. Phys.* **1980**, *72*, 5639−5648.

(20) NIST Standard Reference Database No. 69; NIST: Gaithersburg, MD; http://webbook.nist.gov/chemistry/. Accessed March 15, 2010.

(21) Perdew, J. P.; Chevary, J. A.; Vosko, S. H.; Jackson, K. A.; Pederson, M. R.; Singh, D. J.; Fiolhais, C. *Phys. Rev. B: Condens. Matter Mater. Phys.* **1992**, *46*, 6671−6687.

(22) (a) Evans, D. F. *J. Chem. Soc.* **1957**, 3885−3888. (b) Evans, D. F. *J. Chem. Soc.* **1959**, 2753−2757. (c) Yip, R. W.; Sharma, D. K.; Giasson, R.; Gravel, D. *J. Phys. Chem.* **1984**, *88*, 5770−5772. (d) Lim, E. C.; Chakrabarti, S. K. *J. Chem. Phys.* **1967**, *47*, 4726−4730.

(23) (a) Hajgató, B.; Szieberth, D.; Geerlings, P.; De Proft, F.; Deleuze, M. S. *J. Chem. Phys.* **2009**, *131*, 224321. (b) de Silva, E. C.; Gerratt, J.; Cooper, D. L.; Raimondi, M. *J. Chem. Phys.* **1994**, *101*, 3866−3887.

(24) (a) Čížek, J. *J. Chem. Phys.* **1966**, *45*, 4256−4266. (b) Pople, J. A.; Head-Gordon, M.; Raghavachari, K. *J. Chem. Phys.* **1987**, *87*, 5968−5975.

(25) Kendall, R. A.; Dunning, T. H., Jr.; Harrison, R. J. *J. Chem. Phys.* **1992**, *96*, 6796−6806.

(26) (a) Schröder, D.; Shaik, S.; Schwarz, H. *Acc. Chem. Res.* **2000**, *33*, 139−145. (b) Shaik, S.; Hirao, H.; Kumar, D. *Acc. Chem. Res.* **2007**, *40*, 532−542. (c) Shaik, S.; Filatov, M.; Schröder, D.; Schwarz, H. *Chem.−Eur. J.* **1998**, *4*, 193−199.

(27) Carter, E. A.; Goddard III, W. A. *J. Phys. Chem.* **1988**, *92*, 2109−2115.

(28) In $^2\Phi_{COV}$ one electron from the oxo doubly occupied orbital (corresponding to π_{FeO} in Scheme 3a) is shifted to porphyrin$^{+\bullet}$, while the arene in turn is promoted to a triplet state. As such creating $^2\Phi_{COV}$ is quite energy demanding, and the CT state is dominated by the charge-transfer structures.

(29) Such a CT state as in Fig. 7b was tested by the VB method in the following paper, using the two O-C bonds of oxirane: Chen, Z.; Song, J.; Shaik, S.; Hiberty, P. C.; Wu, W. *J. Phys. Chem. A* **2009**, *113*, 11560−11569.

(30) The deformation energy plays a key role in a related energy decomposition analysis scheme. See: (a) Zeist, W.-J.; Bickelhaupt, F. M. *Org. Biomol. Chem.* **2010**, *8*, 3118−3127. (b) Bickelhaupt, F. M. *J. Comput. Chem.* **1999**, *20*, 114−128. (c) de Jong, G. T.; Bickelhaupt, F. M. *ChemPhysChem* **2007**, *8*, 1170−1181.

(31) Su, P.; Song, L.; Wu, W.; Hiberty, P. C.; Shaik, S. *J. Am. Chem. Soc.* **2004**, *126*, 13539−13549.

(32) Hackett, J. C.; Sanan, T. T.; Hadad, C. M. *Biochemistry* **2007**, *46*, 5924−5940.

(33) Koerts, J.; Boeren, S.; Vervoort, J.; Weiss, R.; Veeger, C.; Rietjens, I. M. C. M. *Chem.-Biol. Interact.* **1996**, *99*, 129−146.